Shearless bifurcations in particle transport for reversed-shear tokamaks

G.C. Grime [1], **M. Roberto**[2], **R.L. Viana** [1,3,†], **Y. Elskens** [4] **and I.L. Caldas**[1]

[1]Institute of Physics, University of São Paulo, São Paulo, SP 05508-090, Brazil

[2]Physics Department, Aeronautics Institute of Technology, São José dos Campos, SP 1228-900, Brazil

[3]Physics Department, Federal University of Paraná, Curitiba, PR 81531-990, Brazil

[4]Aix-Marseille University, UMR 7345 CNRS, PIIM, Campus Saint-Jérôme, Case 322, av. esc. Normandie-Niemen 52, FR-13397 Marseille CEDEX 13, France

Some internal transport barriers in tokamaks have been related to the vicinity of extrema of the plasma equilibrium profiles. This effect is numerically investigated by considering the guiding-centre trajectories of plasma particles undergoing $E \times B$ drift motion, considering that the electric field has a stationary non-monotonic radial profile and an electrostatic fluctuation. In addition, the equilibrium configuration has a non-monotonic safety factor profile. The numerical integration of the equations of motion yields a symplectic map with shearless barriers. By changing the safety factor profile parameters, the appearance and breakup of these shearless curves are observed. The shearless curve's successive breakup and recovery are explained using concepts from bifurcation theory. We also present bifurcation sequences associated with the creation of multiple shearless curves. Physical consequences of scenarios with multiple shearless curves are discussed.

---

1. Introduction

The control of radial particle transport in tokamak plasmas is a necessary, albeit not sufficient, condition for obtaining good confinement, and it is currently an area of intensive research (Hazeltine & Meiss 2003; Horton & Benkadda 2015). Such a goal can be achieved by creating internal transport barriers (ITBs), which are regions of reduced radial (cross-field) particle transport in the plasma column (Horton 2018). Such ITBs have been produced in JET by the utilization of strong supplementary heating during the current rise phase of the plasma discharge (Wolf 2002).

Another type of transport barrier is the so-called edge transport barrier (ETB), related to steep pressure gradients at the plasma edge (Wolf 2002). These gradients arise due to the high pedestal pressure profiles, characteristic of H-mode confinement, and can also exist inside the plasma core (Goldston 1984; Yushmanov *et al.* 1990). This H-mode regime was obtained by combining neutral beam heating with a divertor configuration, showing

a reduction of the particle and energy transport fluxes (Wagner *et al.* 1982; Connor *et al.* 2004).

Recently, a second type of ITB has been investigated, the shearless transport barrier (STB), which appears in tokamak plasmas with reversed-shear profiles, and for which the pressure gradients do not need necessarily to be as large as for ETBs (Caldas *et al.* 2012). Reversed-shear profiles can be obtained by modifying the safety factor profile (Connor *et al.* 2004), and by applying radial electric fields in a specific way (Horton *et al.* 1998). For example, reversed-shear profiles of $q(r)$ have one or more extrema, at which shearless toroidal magnetic surfaces are formed (Morrison 2000). Shearless surfaces represent ITBs in the sense that cross-field transport is reduced therein (Wolf 2002).

Another type of reversed shear appears by a suitable alteration of the tokamak equilibrium, which creates a non-monotonic radial electric field profile (Horton *et al.* 1998; Marcus *et al.* 2019). The presence of ITBs due to this effect can explain the reduction of turbulence-driven particle fluxes observed in tokamak experiments, leading to an improvement of the plasma confinement (Marcus *et al.* 2008). Finally, ITBs have been related to reversed-shear profiles of the toroidal plasma velocity, measured in the Texas Helimak, where a set of probes is mounted to quantify velocity shear in different directions (Gentle *et al.* 2010; Toufen *et al.* 2012).

The STBs are formed in mixed phase space with non-monotonic equilibrium profiles, containing regular particle trajectories as invariant curves and chaotic trajectories (del-Castillo-Negrete, Greene & Morrison 1996). Locally, the invariant curves separate the chaotic trajectories and prevent the global chaotic particle transport in phase space (del-Castillo-Negrete 2000). Moreover, in STBs there are robust curves, namely shearless curves, which survive the increasing of the chaotic area and, consequently, are among the last invariant curves to be broken. This is a dynamical effect due to the perturbed trajectories in non-monotonic plasma profiles (del-Castillo-Negrete *et al.* 1996). The onset of STBs may be one of the mechanisms that hide behind certain improved scenarios observed in tokamaks with non-monotonic plasma profiles. In this work, we apply a model proposed by Horton *et al.* (1998) to show how this mechanism depends on the required profiles.

The presence of different types of reversed shear (safety factor, radial electric field, toroidal plasma velocity) has been investigated by using a drift-wave test particle transport model (Horton *et al.* 1998). The latter is based on $\boldsymbol{E} \times \boldsymbol{B}$ drift combined with the advection of guiding-centre motion along the magnetic field lines (Horton *et al.* 1998). The numerical integration of guiding-centre trajectories leads to a Poincaré stroboscopic map, in which we sample the coordinates at integer multiples of some characteristic period (Lichtenberg & Lieberman 1997). This kind of description, integrating particle trajectories, has led to important advances in the understanding of anomalous particle transport (Horton *et al.* 1998; Kwon *et al.* 2000; El Mouden *et al.* 2007; Rosalem, Roberto & Caldas 2014, 2016; Marcus *et al.* 2019), trapped particle transport (White & Chance 1984) and generic magnetic perturbations (White 2012).

The role of equilibrium profiles and oscillation spectrum in Horton's model has been studied previously. Rosalem *et al.* (2014) investigated the influence of the equilibrium electric field profiles on non-twist transport barriers and reported that monotonic profiles of electric field and safety factor do not generate a STB. Meanwhile, in the plasma edge, the trajectories are mainly determined by the plasma velocity profile (Rosalem *et al.* 2016). The effect of the amplitude of oscillation has also been studied (El Mouden *et al.* 2007; Marcus *et al.* 2019; Osorio *et al.* 2021). However, the influence of the safety factor profile has not yet been systematically investigated.

In this paper, we present a numerical investigation of the formation of single or multiple shearless curves due to reversed magnetic and electric shear profiles. The use of an $E \times B$ drift guiding-centre description allows us to choose the radial profiles for the safety factor, radial electric field and toroidal velocity. In this way, we are able to use reversed-shear profiles in order to study STBs. A numerically obtained Poincaré map is used to compute the rotation number profile, which takes into account all reversed-shear profiles. It turns out that there can be one or more STBs, corresponding to extrema of the rotation number profiles. Shearless curves can be created or destroyed by bifurcations triggered by suitably changing the safety factor profile. We also identify the dynamical mechanisms causing these shearless bifurcations.

This paper is organized as follows. In § 2, we present the drift guiding-centre model to be used in the numerical simulations and the construction leading to the Poincaré map to be used in this work. Section 3 introduces the different reversed-shear profiles to be considered in the numerical simulations, showing the appearance of shearless surfaces at the extrema of rotation number profiles. In § 4, we discuss the possible shearless bifurcation scenarios. Our conclusions are left to the final section.

2. Drift-wave model

One of the characteristic features of anomalous cross-field transport in tokamak plasmas is the presence of electrostatic wave instabilities arising from density and temperature gradients (Horton & Benkadda 2015). A wide spectrum of waves has been shown to produce radial transport fluxes of plasma particles (Horton 2018). A mathematical model for describing the test particle motion in electrostatic waves has been proposed by Horton *et al.* (1998), using a local coordinate system $x = (r, \theta, \varphi)$, where r is the radius measured from the magnetic axis, with θ and φ being the poloidal and toroidal angles, respectively. We denote by a and R, respectively, the minor and major plasma radius.

We consider the combined presence of an equilibrium magnetic field B and an electric field E related to the electrostatic waves. Moreover, let us suppose that the plasma particles are test particles, i.e. they are influenced by the external fields but do not affect them. In the applied model (Horton *et al.* 1998), the ∇B and curvature drifts are neglected, and therefore trapped particle transport is not taken into account. Under these assumptions, the guiding-centre motion has two components: (a) a passive advection along the magnetic field lines, with velocity $v_\parallel$, and (b) an $E \times B$ drift velocity, so that the guiding-centre equation of motion is

$$\frac{\mathrm{d}x}{\mathrm{d}t} = v_\parallel \frac{B}{B} + \frac{E \times B}{B^2}. \tag{2.1}$$

In the large-aspect-ratio approximation ($\epsilon = a/R \ll 1$), we use a tokamak equilibrium magnetic field $B = (0, B_\theta(r), B_\varphi)$, where B_φ and B_θ are the toroidal and poloidal magnetic field components, respectively. Since $B_\theta \sim \epsilon B_\varphi$, we approximate $B \approx B_\varphi \gg B_\theta$ and treat B as a uniform field. The safety factor of the magnetic surfaces is thus given by

$$q(r) = \frac{rB_\varphi}{RB_\theta(r)}. \tag{2.2}$$

The model applied in this paper enables us to relate the advanced scenarios in tokamaks with the STBs predicted for the non-monotonic plasma profiles typical of these scenarios. To investigate this relation, it is assumed in this model (Horton *et al.* 1998) that the electrostatic fluctuation spectrum is coherent and time-independent.

The assumed electric field can be expressed as $E = \bar{E}_r(r) - \nabla\tilde{\phi}$, where $\bar{E}_r$ is a time-independent radial electric field profile and $\tilde{E} = -\nabla\tilde{\phi}$ is a fluctuating part,

representing the electrostatic instabilities in the tokamak edge (Horton *et al.* 1998). The latter is supposed to exhibit a broad spectrum of frequencies $\omega_n = n\omega_0$ and wavevectors, characterized by the oscillation spectrum (Horton *et al.* 1998):

$$\tilde{\phi}(\boldsymbol{x}, t) = \sum_{m,\ell,n} \phi_{m,\ell,n} \cos(m\theta - \ell\varphi - n\omega_0 t \pm \alpha_{m,\ell,n}), \qquad (2.3)$$

where $\alpha_{m,\ell,n}$ is the relative phase and $\phi_{m,\ell,n}$ are constant coefficients. A radial-dependent spectrum was proposed by Connor & Taylor (1987) and results in a global drift-wave map, valid for long times (Kwon *et al.* 2000). However, to study local transport, we use the local drift-wave map, valid for short times (Horton *et al.* 1998). In this local map, we assume the coefficients $\phi_{m,\ell,n}$ to be constants and consider only the dominant spatial mode in (2.3), with harmonics of the lowest angular frequency ω_0, and poloidal and toroidal mode numbers $m = M$ and $\ell = L$, respectively. Although the electrostatic fluctuations have a broad spectrum, the wavenumber width is smaller than the frequency width (Marcus *et al.* 2008). Therefore, the numbers M and L can be estimated by the highest amplitudes in the fluctuation spectrum. In this case, the electrostatic fluctuation spectrum becomes

$$\tilde{\phi}(\boldsymbol{x}, t) = \sum_{n} \phi_n \cos(M\theta - L\varphi - n\omega_0 t + \alpha_n). \qquad (2.4)$$

This model does not take into account the nonlinear interactions between the modes and the incoherent nature of the fluctuations. It supposes a single spatial mode of oscillation and a temporal spectrum concentrated in low frequencies. The correlation time and length of the fluctuation spectrum are key parameters for the validity of this theoretical analysis. If the correlation time τ_c is small compared with the circumnavigation time of the $\boldsymbol{E} \times \boldsymbol{B}$ motion τ_{circ}, then the quasi-linear theory holds. However, if the perturbation has a correlation time long enough for a test particle to be able to feel the whole wave structure, we enter in trapping regime (Diamond, Itoh & Itoh 2010). The dimensionless Kubo number, defined by $K = \tau_c/\tau_{\text{circ}}$, gives us a simple criterion: in the limit $K \ll 1$ the quasi-linear theory holds, and for $K > 1$ the particle is in the trapping regime (Zimbardo, Pommois & Veltri 2000).

Writing (2.1) in components, and taking into account the large-aspect-ratio approximation, yields

$$\frac{\mathrm{d}r}{\mathrm{d}t} = -\frac{M}{Br} \sum_{n} \phi_n \sin(M\theta - L\varphi - n\omega_0 t + \alpha_n), \qquad (2.5)$$

$$r\frac{\mathrm{d}\theta}{\mathrm{d}t} = \frac{rv_\parallel(r)}{Rq(r)} - \frac{\overline{E_r}(r)}{B}, \qquad (2.6)$$

$$R\frac{\mathrm{d}\varphi}{\mathrm{d}t} = v_\parallel(r). \qquad (2.7)$$

The guiding-centre equations of motion (2.5)–(2.7) are written in terms of the three radial profiles to be considered in this work. Defining action and angle variables (Horton *et al.* 1998), $I = (r/a)^2$ and $\psi = M\theta - L\varphi$, and performing a normalization

(Appendix A), the set of three equations reduces to just two:

$$\frac{\mathrm{d}I}{\mathrm{d}t} = 2M \sum_n \phi_n \sin(\psi - n\omega_o t + \alpha_n), \tag{2.8}$$

$$\frac{\mathrm{d}\psi}{\mathrm{d}t} = \epsilon \frac{v_\parallel(I)}{q(I)} [M - Lq(I)] - \frac{M\overline{E_r}(I)}{\sqrt{I}}. \tag{2.9}$$

The drift motion of the guiding centre of charged particles in combined magnetic and electric fields has been long known to be a Hamiltonian system, with canonical equations (Morrison 2000):

$$\frac{\mathrm{d}I}{\mathrm{d}t} = -\frac{\partial H}{\partial \psi}, \quad \frac{\mathrm{d}\psi}{\mathrm{d}t} = \frac{\partial H}{\partial I}, \tag{2.10a,b}$$

where the Hamiltonian can be written as $H(I, \psi, t) = H_0(I) + H_1(\psi, t)$, where

$$H_0(I) = \int^I \mathrm{d}I' \left\{ \epsilon \frac{v_\parallel(I')}{q(I')} [M - Lq(I')] - \frac{M\overline{E_r}(I')}{\sqrt{I'}} \right\} \tag{2.11}$$

is the equilibrium part and

$$H_1(\psi, t) = 2M \sum_n \phi_n \cos(\psi - n\omega_o t + \alpha_n) \tag{2.12}$$

corresponds to the time-dependent perturbation. Hence, in general, the system is non-integrable.

If we switch off the perturbation caused by electrostatic fluctuation (this amounts to setting $\phi_n = 0$ for all values of n), (2.8) shows that the action variable is a constant of motion, as required from an integrable system (Lichtenberg & Lieberman 1997). The perturbations of the quasi-integrable system (2.8)–(2.9) have resonant and non-resonant modes. The resonance condition for a perturbation mode n is given by $(\mathrm{d}/\mathrm{d}t)$ $(\psi - n\omega_0 t) \approx 0$, which implies

$$n\omega_0 = \epsilon \frac{v_\parallel(I)}{q(I)} [M - Lq(I)] - \frac{M\overline{E_r}(I)}{\sqrt{I}}. \tag{2.13}$$

Once the profiles of $q(I)$, $\bar{E}_r(I)$ and $v_\parallel(I)$ are specified, it turns out that (2.13) is satisfied for a given n only for certain values of the action $I = I_n$. From Hamiltonian system theory, it follows that chains of periodic islands appear due to the perturbation, centred at those resonant values I_n.

In order to visualize those islands, we can use a Poincaré map obtained stroboscopically, i.e. we sample the values of the action–angle variables at integer multiples of a characteristic period, which is $\tau = 2\pi/\omega_0$ in our system. Numerically integrating equations (2.8), we obtain stroboscopic Poincaré maps by plotting the trajectories in instants $t_j = j(2\pi/\omega_0)$. The two-dimensional map $I_{j+1} = I_{j+1}(I_j, \psi_j)$, $\psi_{j+1} = \psi_{j+1}(I_j, \psi_j)$ is area-preserving because of the Liouville theorem (Hazeltine & Meiss 2003).

Since we are interested chiefly in non-monotonic radial profiles corresponding to reversed-shear quantities like $q(I)$, $v_\parallel(I)$ and $E_r(I)$, the Poincaré map is non-twist, i.e.

the equilibrium Hamiltonian H_0 has a point where

$$\frac{\partial^2 H_0}{\partial I^2} = 0. \tag{2.14}$$

Many results of the Hamiltonian theory, like Kolmogorov–Arnold–Moser theory and Aubry–Mather theory, hold only for twist systems, and hence new features are expected when non-twist maps are considered (del-Castillo-Negrete *et al.* 1996; Morrison 2000). One of them is the existence of twin island chains (del-Castillo-Negrete *et al.* 1996; Morrison 2000). These twin chains are centred at resonant values I_n satisfying (2.13) that arise in pairs. The evolution of map orbits near twin chains has been extensively investigated for the so-called standard non-twist map (SNM).

Introducing reversed-shear profiles in this model, transport barriers correspond to shearless invariant curves in phase space, defined by an extreme point in rotation number profile (del-Castillo-Negrete *et al.* 1996; Morrison 2000). To every regular (non-chaotic) orbit we can associate a rotation number Ω given by the mean rotation angle in the Poincaré section. Given an initial condition (I_0, ψ_0), the rotation number of this orbit is given by

$$\Omega(I_0) = \lim_{N \to \infty} \frac{\psi_N - \psi_0}{N}, \tag{2.15}$$

where ψ_N is the angle of the Nth intersection in the Poincaré map. We choose $\psi_0 = 0$ in numerical simulations, but the final value does not depend on that choice. The limit in (2.15) exists provided the orbit is non-chaotic.

3. Breakup and reappearance of STBs

In this section, we show the presence of shearless invariant curves locally separating the chaotic trajectories and preventing plasma edge transport.

In order to numerically solve (2.8)–(2.9) we use parameters of TCABR (Nascimento *et al.* 2005), although the results can be applied to any tokamak, described in a large-aspect-ratio approximation. However, we present a conceptual investigation rather than detailed comparisons with experiments performed in any tokamak.

The improvement of plasma confinement quality by using reversed-shear profiles has long been acknowledged. A substantial reduction of the turbulent transport levels has been observed in regions with negative magnetic shear (Mazzucato *et al.* 1996; Connor *et al.* 2004). In order to generate negative shear regions, it is necessary that the safety factor radial profile be non-monotonic. Magnetohydrodynamics-based models of a cylindrical plasma column suggest the following profile of the safety factor (Kerner & Tasso 1982):

$$q(r) = q_a \frac{r^2}{a^2} \left[1 - \left(1 + \mu' \frac{r^2}{a^2} \right) \left(1 - \frac{r^2}{a^2} \right)^{\nu+1} \right]^{-1}, \tag{3.1}$$

where q_a is the safety factor at the plasma edge and

$$\mu' = \mu \frac{\nu + 1}{\mu + \nu + 2}. \tag{3.2}$$

In the numerical simulations shown in this work, we fixed the parameters $\nu = 0.8$ and $q_0 = 3.75$, making the remaining parameter μ a function of q_a, which we choose as our control parameter. Such a high value of q_0 is not usual in common discharges but is present in strong reversed magnetic shear profiles for studies in ITER (Sips *et al.* 2005;
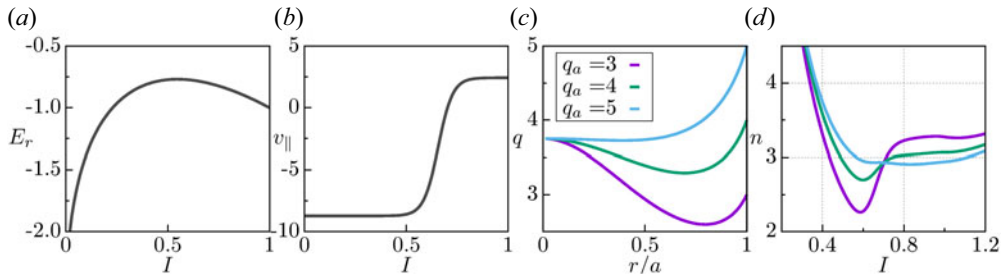
FIGURE 1. Profiles of (*a*) radial electric field, (*b*) parallel velocity, (*c*) non-monotonic safety factor profile and (*d*) resonant mode numbers as a function of the action value for different values of q_a. Since only integer values of n are allowed, it follows that only the modes $n = 3$ and 4 produce resonances.

Joffrin 2007). The $q(r)$ profile is plotted in figure 1(*c*) for some values of the control parameter. For $q_a = 3$ and 4, the profile is non-monotonic, with minima at $r/a \approx 0.7$ and 0.8, respectively; whereas $q_a = 5$ yields a quasi-monotonic profile, included here for completeness. This range of values of q_a is compatible with TCABR plasma discharges (Nascimento *et al.* 2005).

The presence of negative shear in the radial electric field profile has been related to the reduction of turbulent particle fluxes in H-mode tokamak discharges (Viezzer *et al.* 2013). This effect is compatible with a STB if the radial profile of E_r is non-monotonic (Marcus *et al.* 2008, 2019). One of the simplest functions with this property is a quadratic one, given by

$$\overline{E_r}(r) = 3\alpha r^2 + 2\beta r + \gamma, \quad (3.3)$$

where $\alpha = -1.14$, $\beta = 2.529$ and $\gamma = -2.639$ are parameter values after normalization (see Appendix A for details). These values were chosen to yield a local minimum in the desired plasma region and are compatible with profiles measured in the TCABR tokamak (Nascimento *et al.* 2005).

Toroidal plasma rotation is an important effect to be taken into account in tokamaks, such as stabilization or growth rate decrease of certain magnetohydrodynamic modes. Besides intrinsic rotation, this effect can also be obtained by using neutral beam injection, since the incident particles impart momentum to the plasma particles. Moreover, it has been observed that plasma rotation is able to decrease turbulent flux levels in the plasma edge (Gentle *et al.* 2010; Toufen *et al.* 2012). Hence, it has been conjectured that non-monotonic profiles of the toroidal plasma velocity can be related to ITBs (actually, shearless barriers).

Spectroscopic techniques have been used for the measurement of toroidal plasma rotation velocities in TCABR discharges, giving values of about $3.0 \, \text{km} \, \text{s}^{-1}$ for the plasma edge (Nascimento *et al.* 2005). A normalized parallel velocity profile used in this work, and consistent with TCABR observations, is given by

$$v_{\parallel}(I) = v_{\parallel 0} + v_m \tanh(\sigma_1 I + \sigma_2), \quad (3.4)$$

where the parameters take the following values: $v_{\parallel 0} = -3.15$, $v_m = 5.58$, $\sigma_1 = 14.1$ and $\sigma_2 = -9.26$, once we apply the normalization factor $v_0 = E_0/B_0$ (Osorio *et al.* 2021). Profiles of E_r and $v_{\parallel}$ are shown in figure 1(*a*,*b*).

After discussing the equilibrium aspects of the model, let us consider the perturbation caused by the electrostatic fluctuations given by (2.4). We assume the spatial dominant
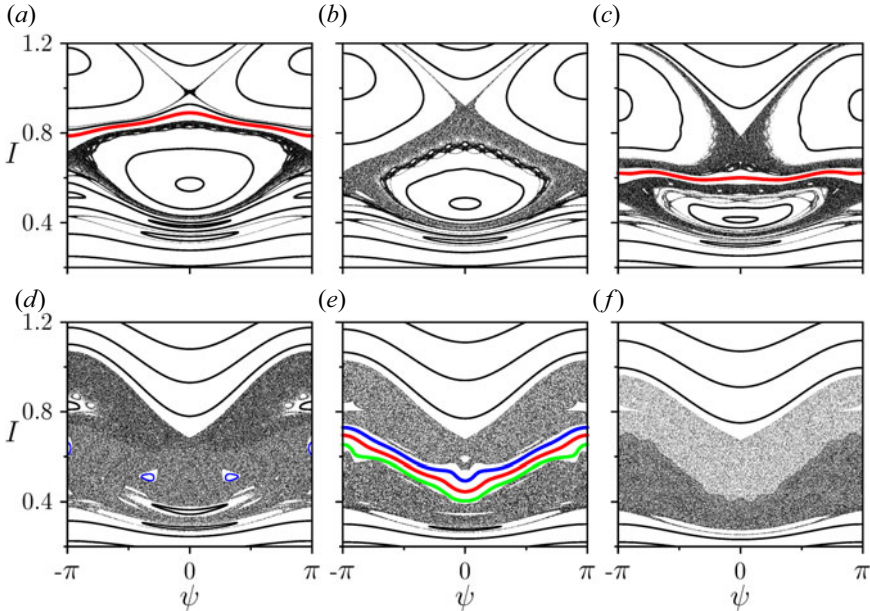
FIGURE 2. Poincaré sections in the action–angle variables obtained by numerical integration of the equations of drift motion, for different values of the safety factor at plasma edge: (a) $q_a =$ 5.00, (b) $q_a = 4.50$, (c) $q_a = 4.00$, (d) $q_a = 3.45$, (e) $q_a = 3.30$ and (f) $q_a = 3.00$. The shearless curves are indicated by green, red and blue wherever they appear in the Poincaré sections.

mode to have $M/L = 16/4$, which are typical numbers in the wave spectrum at the tokamak plasma edge (Horton *et al.* 1998). The temporal modes considered are $n =$ 2, 3, 4, based on the fluctuating spectrum of TCABR (Marcus *et al.* 2008), with normalized amplitudes $\phi_2 = 11.74 \times 10^{-3}$, $\phi_3 = 2.077 \times 10^{-3}$ and $\phi_4 = 0.2443 \times 10^{-3}$. The fundamental frequency of the temporal modes is around 10 kHz (Marcus *et al.* 2019), which implies a normalized angular frequency $\omega_0 = 5.224$. We keep $\alpha_n = 0$ and the perturbation amplitudes at these values throughout this work.

Assuming that the rest of the profiles and parameters are fixed, the safety factor is chosen to be the tunable parameter which determines the dynamical behaviour of the system. Given a q_a value, as mentioned before, there are resonant actions I_n determined by the condition (2.13), whose numerical solution is shown in figure 1(*d*) for different values of q_a. The mode $n = 3$ produces a resonance at two values of the action $I_{3,(a,b)}$, which also characterizes non-twist behaviour. The $n = 4$ mode, however, gives a resonance at a single value I_4. In addition, the $n = 2$ mode does not yield resonance at any value of I, but it nevertheless influences the formation and destruction of STBs (Marcus *et al.* 2019).

The variation of the safety factor profile changes the behaviour of STBs. Figure 2 displays examples of Poincaré sections for some values of control parameter q_a. We represent the action–angle variables as rectangular coordinates for better visualization. In figure 2(*a*), obtained for $q_a = 5.00$, we observe two large (twin) islands and a chaotic region around the inner one (the outer island has also a chaotic region, but it is too narrow to be seen with the present resolution).

Those islands refer to the main resonances of $n = 3$ mode in figure 1 and are direct consequences of the non-monotonicity of the profiles. Between these twin islands, there is a shearless curve, located at the action value corresponding to an extremum of the rotation
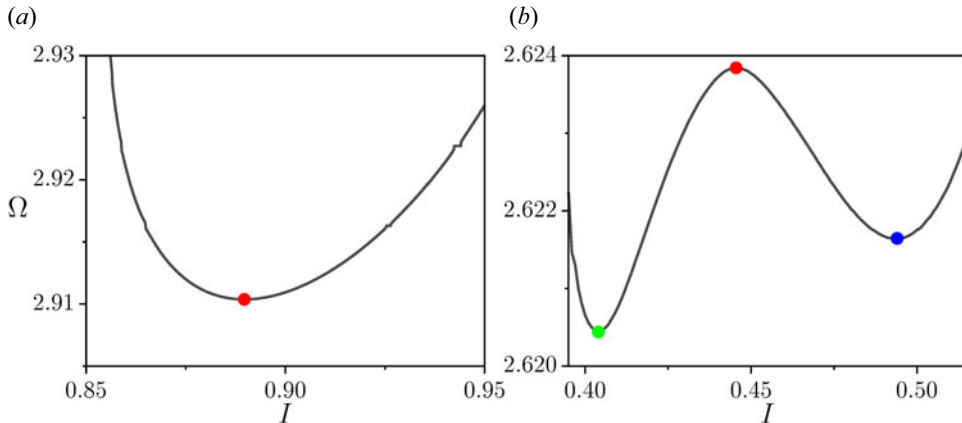
FIGURE 3. Rotation number profiles corresponding to the Poincaré sections depicted in figures 2(*a*) and 2(*e*). The extrema for each case are indicated by red, green and blue points, in the case of one, two and three coexisting shearless curves, respectively.

number profile (figure 3*a*). There are other island chains corresponding to higher-order resonances, but their width is considerably smaller than the main ones, and their effect will not be taken into account, at least not directly.

The chaotic region around the inner islands grows as the parameter q_a decreases and eventually causes the breakup of the shearless curve for $q_a = 4.50$ (figure 2*b*). The mechanism of shearless curve breakup due to increasing perturbation has been thoroughly described by Morrison and co-workers, in the context of the SNM, introduced by del-Castillo-Negrete *et al.* (1996):

$$I_{n+1} = I_n - \tilde{b} \sin(2\pi\theta_n), \tag{3.5}$$

$$\theta_{n+1} = \theta_n + \tilde{a}(1 - I_{n+1}^2), \tag{3.6}$$

where (I_n, θ_n) can be regarded as action–angle variables of the drift model when we consider a quadratic approximation of the radial safety factor profile about a local extremum (Horton *et al.* 1998), and $\tilde{a}$, $\tilde{b}$ are system parameters. In this work, we vary the equilibrium magnetic field configuration while keeping constant the perturbation amplitude. Furthermore, we find new scenarios for the shearless curve onset and breakup. Moreover, a map (discrete-time) model can be obtained if we consider a wide frequency spectrum of equally spaced resonant modes, instead of a single dominant resonant mode.

Of note, if the value of q_a is further decreased to 4.00, the shearless curve between the two twin islands reappears (figure 2*c*), since the corresponding rotation number profile has an extremum for this parameter value. This new shearless curve, on its way, is broken for smaller values of q_a, like 3.45 (figure 2*d*).

Further decrease in q_a causes the appearance of three shearless curves at $q_a = 3.30$ (plotted in red, green and blue in figure 2*e*). They are also located at extrema of the rotation number profile: the red one at a maximum, and the green and blue ones at minima (figure 3*b*). These multiple shearless curves also disappear for even lower values of q_a, as exemplified by figure 2(*f*), obtained for $q_a = 3.00$. In this Poincaré map, we can see that even after the shearless curve breakup a partial transport barrier persists, as seen by the density of points, due to the stickiness effect.

The stickiness phenomenon occurs when a chaotic orbit in the vicinity of periodic island chains spends a large amount of time encircling it, after which it is free to diffuse until it approaches the neighbourhood of another periodic orbit, where it may be trapped again, and so on. This results in an anomalous diffusion scenario, whereby the orbit experiences long periods of trapping, interspersed by fast diffusion in the chaotic sea. This trapping near a periodic island is attributed to the existence of cantori, or tori perforated in a self-similar way, and the stickiness-induced trapping can be quantified by the calculation of the finite-time Lyapunov exponents (Szezech *et al.* 2009). The mechanism for orbit escape through cantori involves a structure called turnstiles, formed by segments of invariant manifolds of unstable periodic orbits embedded in the chaotic sea (MacKay, Meiss & Percival 1984).

A related investigation, reported in Szezech *et al.* (2012), quantifies the transport properties of the SNM, due to the STB, using a novel concept, the finite-time rotation number, which is computed in the same way as the conventional rotation number, but using a short period of time. The statistical properties of the finite-time rotation number are remarkably similar to those of the finite-time Lyapunov exponents. For example, Lagrangian coherent structures (LCS) can be obtained by considering the ridges of the scalar field of the finite-time rotation number, over a given phase space region. The LCS are structures that have properties similar to those of the invariant manifolds of periodic orbits but, unlike the latter, are defined in more general contexts (e.g. when there is explicit time dependence), which allows their use in a wide variety of plasma physics applications (Falessi, Pegoraro & Schep 2015). In addition, LCS can also be interpreted as transport barriers, and their description reveals escape patterns for the $E \times B$ motion of plasma particles.

Sequences of breakup and reappearance of shearless curves as a parameter is varied, exemplified by figure 2(*a–c*), occur quite often in the non-twist system considered in this work. In figure 4 we plot a shearless bifurcation diagram, showing the extrema of rotation number as a function of the parameter q_a. Hence, each point in this diagram corresponds to a shearless curve, whenever it exists. There are some gaps in the diagram, corresponding to parameter values with no extrema of Ω, or for which the rotation number itself is ill-defined (because the considered orbit is chaotic, for example). Such regions are indicated in black in the bar at the top of figure 4.

For most parameter values in the shearless bifurcation diagram, there is only one shearless curve, represented by red points in figure 4, corresponding to the red regions in the colour bar. Multiple shearless curves are indicated by blue and green points, when there are two and three coexisting shearless curves, respectively. In the inset of figure 4 we display a magnification of the interval $3.1 < q_a < 3.4$, for which there are green points indicating three coexisting shearless curves. There are some blue points as well, but they occupy a region so small that they are barely visible in figure 4.

We see that a shearless bifurcation is an abrupt change in the behaviour of the shearless curve as a system parameter is varied through a critical value. For example, a change between red and green points in figure 4 suggests the occurrence of a shearless bifurcation, whereby a single shearless curve bifurcates into two shearless curves as the parameter q_a passes through some value. When green points become red points again, we can speak of an inverse shearless bifurcation. Bifurcations on transport barriers like the one mentioned above were experimentally observed for JET and ASDEX Upgrade (Joffrin *et al.* 2003). However, in these experiments, the triggering mechanism of those barriers is different from the one presented in this paper, but the possibility of having more than one transport barrier remains.
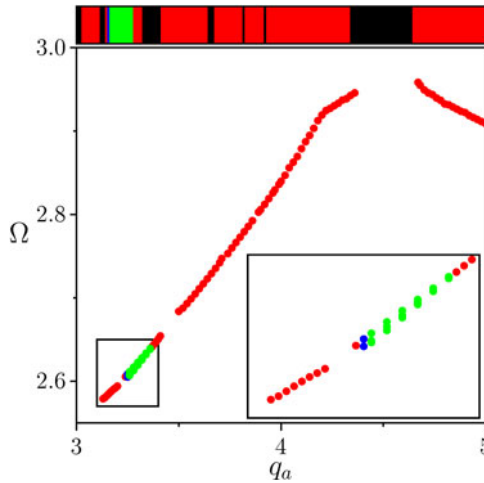
FIGURE 4. Shearless bifurcation diagram showing the extrema of the rotation number profile (whenever they exist) as a function of the control parameter q_a. Blue and green points indicate the observation of two and three extrema, respectively. In the top colour bar, black regions represent intervals for which there is no shearless curve.

4. Shearless bifurcation scenarios

The shearless curves undergo bifurcations of many types. In the most frequent, the shearless curve simply disappears as a control parameter passes through some critical value. Since shearless curves represent transport barriers, their breakup will be followed by a significant increase in the transport levels (Szezech *et al.* 2009). After the breakup of a shearless curve, a larger chaotic region would enable the guiding centres to undergo longer excursions in action space (Szezech *et al.* 2009). However, if limited regions of chaotic orbits exist before the shearless curve breaks down, the curve breakup is not expected to increase significantly the transport levels.

In the SNM, after the shearless curve disappears, global chaotic transport appears in phase space, since at both sides of the shearless curve there are locally chaotic regions that merge together after the curve breakup, leaving a larger chaotic region therein. We observed that the system (2.8)–(2.9) manifests some atypical shearless breakups. Two of them are shown in figures 5 and 6. Each one depicts a shearless breakup in one of the reconnection scenarios of the SNM.

Figure 5 shows an odd reconnection scenario involving the shearless curve. Figure 5(*a*) displays the shearless curve (in red) located between twin chains of 19 islands each (in cyan and magenta), evident in the magnification of the rectangle area (figure 5*b*). A slight decrease in the value of the control parameter q_a leads to a collision of both island chains with the shearless curve and, in this process, the STB breaks up (figure 5*c*). A further decrease in q_a causes the reappearance of a shearless curve in a meandering form, separating the two island chains (figure 5*d*). Lowering further the parameter q_a, this odd reconnection scenario involves the extinction of the twin islands, leaving only the meandering invariant curves, separated by the surviving shearless curve (figure 5*e*).

A sequence of Poincaré sections showing an even reconnection scenario is depicted in figure 6. For a given value of q_a there are twin chains of four islands each (marked green and blue), straddling a shearless curve (in red) (a magnification of the phase portrait, showing only two islands in each chain, is displayed in figure 6*a*). For the current value of
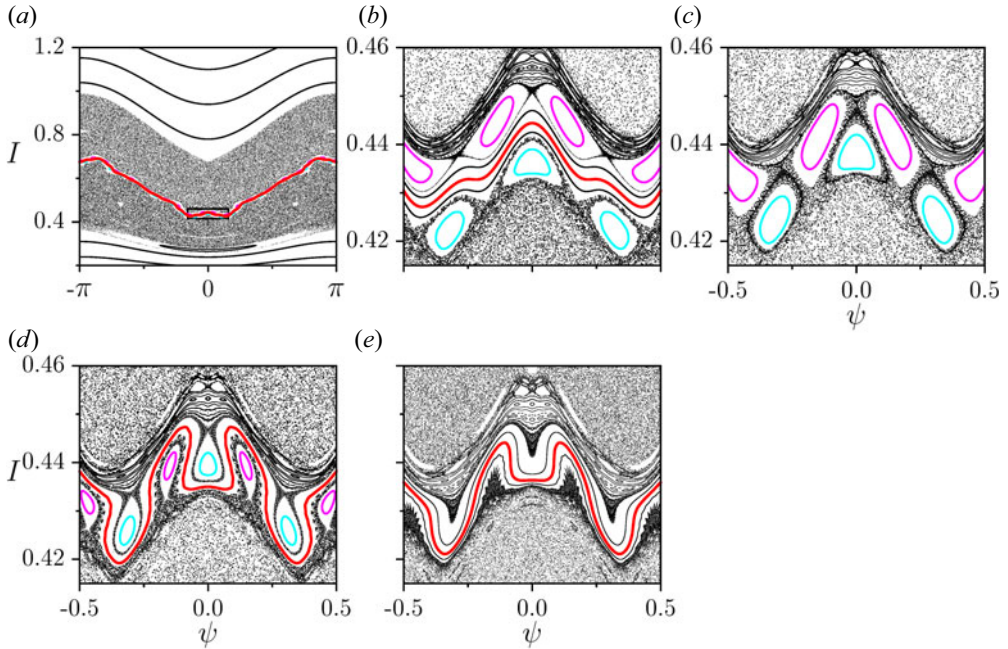
FIGURE 5. Poincaré sections of the drift-wave model for (*a*) $q_a = 3.1290$, (*b*) magnification of marked region in (*a*), (*c*) $q_a = 3.1282$, (*d*) $q_a = 3.1277$ and (*e*) $q_a = 3.1272$. The remaining parameter values are the same as in figure 2. In these phase portraits, we magnify the region containing the twin islands of 19 islands each, straddling the shearless curve.

the amplitudes considered in this figure, there are already two sizeable chaotic regions on both sides of the shearless curve, where the remnants of the islands are embedded.

As the control parameter q_a slightly increases, the twin island chains approach each other and reconnect, causing a transition when the shearless curve is absent (figure 6*b*), although the STB is still present. Increasing again q_a, the lower island chain (green) disappears, leaving only the upper chain (blue), showing an asymmetry characteristic of this even reconnection scenario (figure 6*c*). After this remaining island disappears, for increasing q_a, the shearless curve reappears (figure 6*d*). The asymmetric behaviour of this even reconnection scenario is a characteristic of non-twist maps with a lack of symmetry, such as the considered model. For example, the SNM (3.5) has symmetry with respect to action coordinate (del-Castillo-Negrete *et al.* 1996). However, most other maps do not have such property, like the extended SNM (Wurm & Martini 2013).

Another category of shearless bifurcations concerns the appearance of more than one shearless curve, as illustrated by figure 7. For $q_a = 3.2360$ there are four island chains, two of them at each side of a shearless curve, marked in magenta, blue, green and cyan. As in the previous figure, the amplitude of the perturbation is already large enough to create two large chaotic regions at each side of the shearless curve, which acts as a transport barrier, in this case preventing large-scale excursion of particles in chaotic orbits.

Let us consider the vicinity of one island of the magenta chain in more detail, as revealed by the magnification shown in figure 7(*b*). On changing the control parameter value, the periodic points of the chain collide and a chaotic layer takes their place, containing a myriad of islands (figure 7*c*). This collision represents a saddle–centre bifurcation: we have pairs of periodic points, half of them locally stable (centres) and the other half unstable
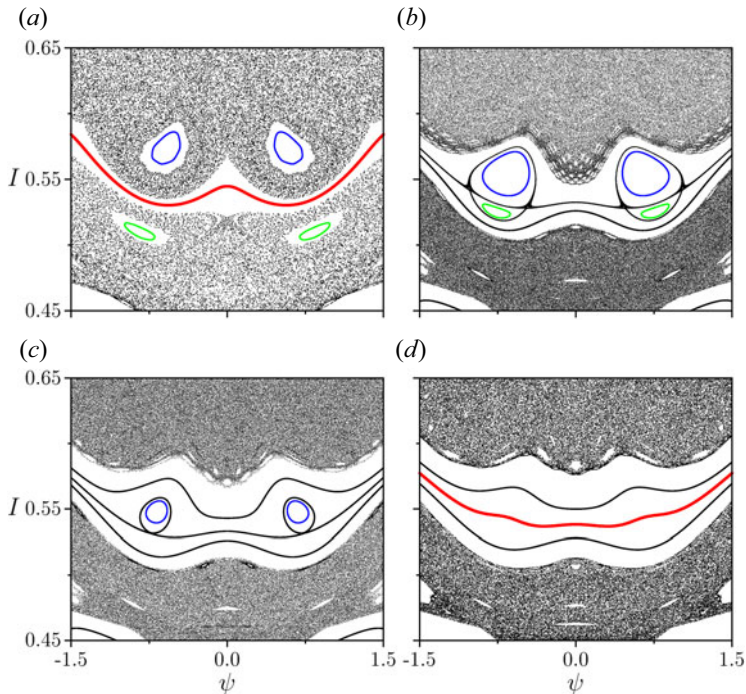
FIGURE 6. Poincaré sections of the drift-wave model for (*a*) $q_a = 3.700$, (*b*) $q_a = 3.725$, (*c*) $q_a = 3.730$ and (*d*) $q_a = 3.740$. The remaining parameter values are the same as in figure 2.

(saddles). As the control parameter increases, these pairs of periodic points approach each other and eventually coalesce at the bifurcation points, disappearing afterwards, and leaving a chaotic layer therein. In this myriad of islands there is a pair of twin island chains, with 73 islands each marked in gold and pink, having the same rotation number (figure 7*d*). A bifurcation process extinguishes those twin island chains and generates a second shearless curve, plotted in blue in figure 7(*e*). Finally, figure 7(*f*) displays the full scenario with the two shearless curves. We remark that the appearance of the second shearless curve is a bifurcation in the rotation number profile, whereas the saddle–centre (O–X) bifurcation which precedes the latter occurs in phase space (here represented by Poincaré sections). Bifurcations of this type have been observed in some atypical scenarios in the SNM (Wurm *et al.* 2005).

The process detailed in figure 8 is analogous to figure 7 and leads to a third shearless curve, through the same kind of shearless bifurcation. In figure 8(*a*), obtained for $q_a = 3.2451$, we show a scenario just after the appearance of a second shearless curve, straddling two chaotic regions. In this Poincaré section, below the shearless curve, there is a chain of five tiny islands, one of which is magnified and shown in cyan in figure 8(*b*). Starting from this island (as well as the other ones in the same chain), a third shearless curve emerges, which is plotted in green in figure 8(*c*). In this example, another saddle–centre bifurcation occurs in the Poincaré section, leading to secondary twin island chains with 58 islands each (not shown in the figure), which precedes the shearless bifurcation causing the emergence of the third shearless curve. The scenario after the emergence of the green shearless curve is depicted in figure 2(*e*).

The last scenario of shearless bifurcation presented in this paper is shown in figure 9. For $q_a = 3.365$ we see, in the Poincaré section, three shearless curves, marked in blue, red and
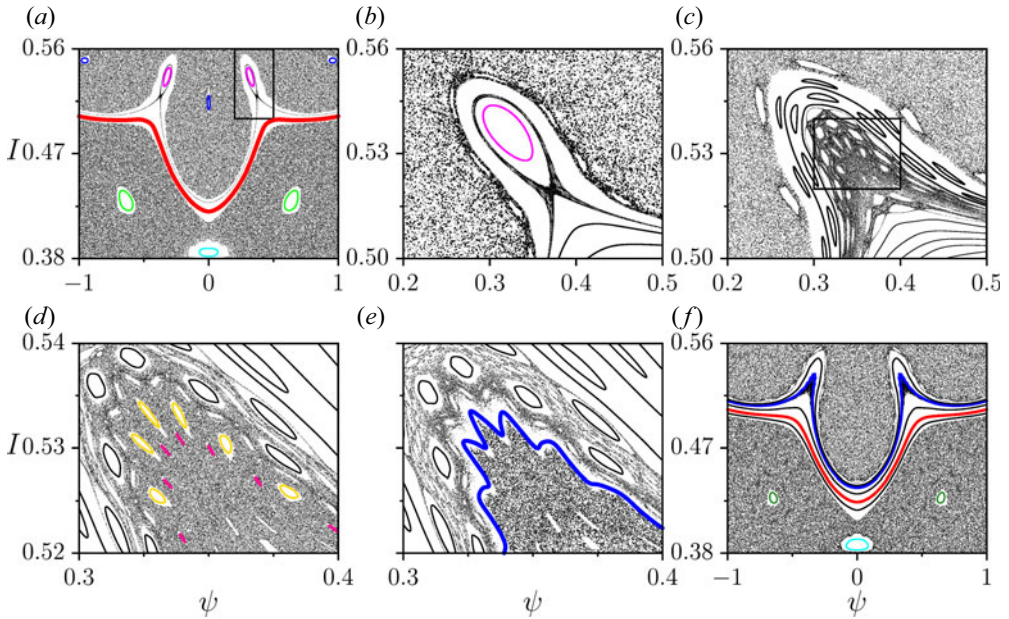
FIGURE 7. Poincaré sections of the drift-wave model for (*a*) $q_a = 3.2360$, (*b*) magnification of a region of (*a*), (*c*) $q_a = 3.23841$, (*d*) magnification of a region of (*c*) and (*e*) $q_a = 3.23849$. (*f*) A zoom out of (*e*). The remaining parameter values are the same as in figure 2. This sequence represents a scenario containing four isochronous chains (magenta, cyan, blue and green) originating shearless bifurcations. The periodic points of the magenta chain, in (*a,b*), collide in a saddle–centre bifurcation (*c*) and a second shearless curve arises in (*d*) after the suppression of pink and gold twin island chains, containing 73 islands each (*e*).
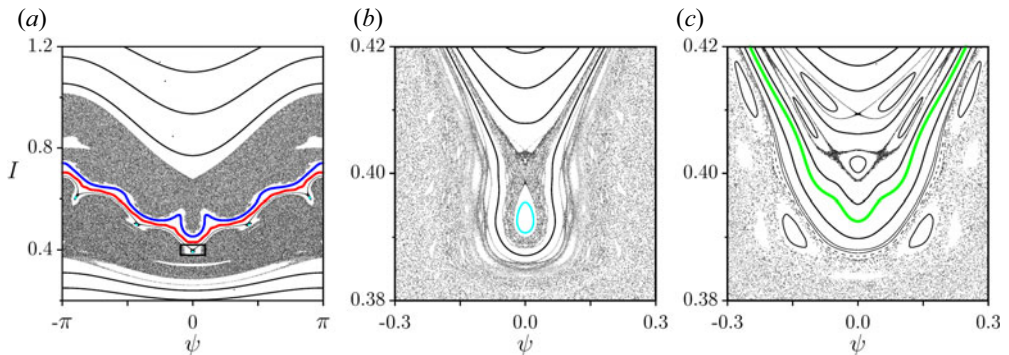

FIGURE 8. Poincaré sections of the drift-wave model for (*a*) $q_a = 3.2451$, (*b*) magnification of a region of (*a*) and (*c*) $q_a = 3.2527$. The remaining parameter values are the same as in figure 2. This scenario illustrates the emergence of a third shearless curve through a saddle-node bifurcation.

green (figure 9*a*). The rotation number profile corresponding to this case (figure 9*c*) has three extrema: one maximum, corresponding to the red shearless curve, and two minima, corresponding to the green and blue curves. As the control parameter increases slightly, the red and blue shearless curves collide at a critical value of q_a. After the collision, these shearless curves mutually annihilate, leaving only the green shearless curve (figure 9*b*), as
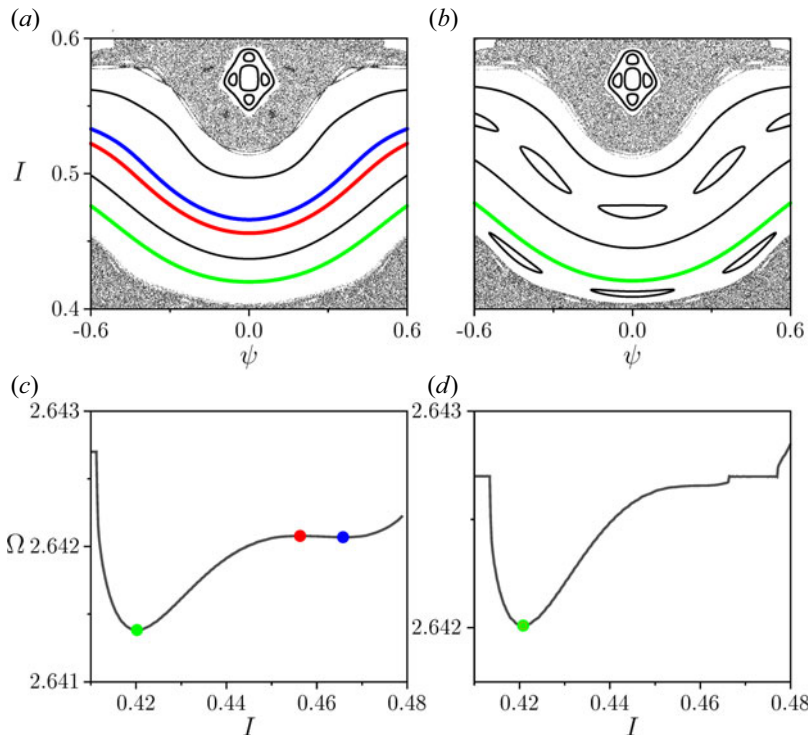
FIGURE 9. Poincaré sections of the drift-wave model: (*a*) magnification of a region when $q_a = 3.365$; (*b*) magnification of a region when $q_a = 3.367$. Rotation number profile for (*c*) $q_a = 3.365$ and (*d*) $q_a = 3.367$. The remaining parameter values are the same as in figure 2. This scenario exemplifies a bifurcation of shearless curves by collisions of periodic points (saddle–centre). The red and blue curves collide and mutually annihilate.

confirmed by the rotation number profile for this value of q_a (figure 9*d*), which exhibits only the minimum corresponding to the green shearless curve.

5. Conclusions

Shearless transport barriers have been identified in a theoretical model describing the $E \times B$ drift motion of the guiding centres. These barriers may be one of the mechanisms that hide behind certain improved scenarios observed in tokamaks with non-monotonic plasma profiles. Three profiles have been specified in advance, following experimental evidence: the safety factor radial profile, the average radial electric field profile and the toroidal velocity profiles. Excepting toroidal velocity, those profiles are non-monotonic and thus present some kind of reversed shear, the combined effect of them being the key ingredient in our model.

The equilibrium configuration characterized by these non-monotonic profiles is perturbed by the influence of electrostatic fluctuations with a dominant mode, whose amplitude was also determined from experimental results for the TCABR tokamak. Our results follow by numerical integration of the drift motion equations taking into account the reversed-shear profiles as well as the electrostatic fluctuation field. Since the motion equations were expressed in action–angle variables, the drift motion has a Hamiltonian form, and the Poincaré sections (taken at integer multiples of the dominant mode of the perturbation period) are actually area-preserving maps of a non-integrable system.

Since the radial profiles used are non-monotonic, this is a non-twist system, and hence some novel features are expected with respect to models using monotonic profiles. One of them is the existence of shearless curves, located at extrema of the rotation number profiles (in action space, which is essentially the radial direction).

The main result of our work was the discovery of multiple shearless curves when one of the system parameters (namely the safety factor at the plasma edge) is varied in specified intervals. These intervals comprise the neighbourhood of $q_a = 3$ equilibrium magnetic surface and thus are of physical interest since many tokamaks (including TCABR) operate at that range. Such multiple shearless curves can appear and disappear due to shearless bifurcations since they occur after (or before) the control parameter passes through critical values.

We identified three groups of shearless bifurcations. In the first group, we have shearless curves that simply break up and reappear, indicating local changes in the rotation number profile (figures 5 and 6). Additionally, a partial transport barrier may still persist after the shearless curve breakup. In fact, small variations in the system parameters affect substantially the transport coefficients in such situations due to the configuration of cantori, LCS and escape channels by turnstiles. Furthermore, other mechanisms are relevant for the reduction of transport coefficients of non-twist systems, such as manifold crossing.

In the second bifurcation group, new shearless curves appear in phase space, after a saddle–centre bifurcation and the emergence of secondary twin island chains (figures 7 and 8). These curves are related to extrema of the rotation number profile, but one of them corresponds to a local minimum, while the other one to a local maximum. Finally, the third group involves the collision and disappearance of shearless curves, due to a bifurcation in the rotation number profile (figure 9) characterized by maximum and minimum points colliding as the control parameter is varied.

Depending on the strength of the fluctuation amplitudes, Poincaré sections show the existence of chaotic orbits on both sides of the shearless curves, indicating a limited extension of the chaotic transport in this region. In this case, when a shearless barrier breaks up, the chaotic orbits often merge together, leading to global transport. If there is more than one shearless curve, however, we can have two regions where the chaotic transport is reduced, increasing the complexity of the description. Since multiple ITBs have been actually verified experimentally, our work sheds some light on the nature of this dynamic phenomenon.

Acknowledgements

Funding

Declaration of interests

The authors report no conflict of interest.

Appendix A. Normalization of variables in the drift-wave model

In this appendix, we outline the normalization of variables of the drift-wave model used in this paper, namely B, a, ω_0, $\overline{E_r}$, ϕ_n and $v_{\parallel}$. Note that SI units are used throughout. The minor plasma radius, a, is divided by the factor $a_0 = 0.18$ m, so the normalized value $a' = a/a_0 = 1$. Besides the normalization of the plasma radius, the TCABR tokamak aspect ratio $\epsilon = 0.3$ is maintained. The same is done for the toroidal field: we choose $B_0 = 1.1$ T $\Rightarrow B' = B/B_0 = 1$. We adopt an electric field normalization factor so that its magnitude has a unit absolute value at the plasma edge: $E_0 = |\overline{E_r}(r = a)|$. Here

$$\overline{E_r} = 3\alpha r^2 + 2\beta r + \gamma, \tag{A1}$$

where $\alpha = -80 \, \text{kV m}^{-3}$, $\beta = 31.95 \, \text{kV m}^{-2}$ and $\gamma = -6 \, \text{kV m}^{-1}$. Thus, $E_0 = 2274 \, \text{V m}^{-1}$ and the normalized field, in action variables, is

$$\overline{E_r}' = \frac{\overline{E_r}}{E_0} = 3\frac{\alpha a^2}{E_0}\left(\frac{r}{a}\right)^2 + 2\frac{\beta a}{E_0}\left(\frac{r}{a}\right) + \frac{\gamma}{E_0}; \tag{A2}$$

therefore,

$$\overline{E_r}' = 3\alpha'I + 2\beta'\sqrt{I} + \gamma', \tag{A3}$$

with $(\alpha', \beta', \gamma') = (-1.140, 2.529, -2.639)$.

The velocity, time and electric potential normalization factors are given by $v_0 = E_0/B_0 = 2067 \, \text{m s}^{-1}$, $t_0 = a_0/v_0 = 8.707 \times 10^{-5} \, \text{s}$ and $\phi_0 = a_0E_0 = 409.3$ V, respectively, whereas the lowest angular frequency is $\omega_0 = 6 \times 10^4 \, \text{rad s}^{-1}$, such that its normalized value is given by $\omega_0' = \omega_0 t_0 = 5.224$.

REFERENCES

CALDAS, I.L., VIANA, R.L., ABUD, C.V., FONSECA, J.C.D., GUIMARÃES FILHO, Z.O., KROETZ, T., MARCUS, F.A., SCHELIN, A.B., SZEZECH JR., J.D. & TOUFEN, D.L. 2012 Shearless transport barriers in magnetically confined plasmas. *Plasma Phys. Control. Fusion* **54**, 124035.

DEL-CASTILLO-NEGRETE, D. 2000 Chaotic transport in zonal flows in analogous geophysical and plasma systems. *Phys. Plasmas* **7**, 1702.

DEL-CASTILLO-NEGRETE, D., GREENE, J.M. & MORRISON, P.J. 1996 Area preserving nontwist maps: periodic orbits and transition to chaos. *Physica* D **91**, 1.

CONNOR, J.W., FUKUDA, T., GARBET, X., GORMEZANO, C., MUKHOVATOV, V. & WAKATANI, M. 2004 A review of internal transport barrier physics for steady-state operation of tokamaks. *Nucl. Fusion* **44**, R1.

CONNOR, J.W. & TAYLOR, J.B. 1987 Ballooning modes or Fourier modes in a toroidal plasma? *Phys. Fluids* **30**, 3180.

DIAMOND, P.H., ITOH, S.-I. & ITOH, K. 2010 *Modern Plasma Physics*. Cambridge University Press.

EL MOUDEN, M., SAIFAOUI, D., ZINE, B. & EDDAHOY, M. 2007 Transport barriers with magnetic shear in a tokamak. *J. Plasma Phys.* **73**, 439.

FALESSI, M.V., PEGORARO, F. & SCHEP, T.J. 2015 Lagrangian coherent structures and plasma transport processes. *J. Plasma Phys.* **81**, 495810505.

GENTLE, K.W., LIAO, K., LEE, K. & ROWAN, W.L. 2010 Comparison of velocity shear with turbulence reduction driven by biasing in a simple cylindrical slab plasma. *Plasma Sci. Technol.* **12**, 391.

GOLDSTON, R.J. 1984 Energy confinement scaling in Tokamaks: some implications of recent experiments with Ohmic and strong auxiliary heating. *Plasma Phys. Control. Fusion* **26**, 87.

HAZELTINE, R.D. & MEISS, J.D. 2003 *Plasma Confinement*. Dover.

HORTON, W. 2018 *Turbulent Transport in Magnetized Plasmas*. World Scientific.

HORTON, W. & BENKADDA, S. 2015 *ITER Physics*. World Scientific.

HORTON, W., PARK, H.B., KWON, J.M., STROZZI, D., MORRISON, P.J. & CHOI, D.I. 1998 Drift wave test particle transport in reversed shear profile. *Phys. Plasmas* **5**, 3910.

JOFFRIN, E. 2007 Advanced tokamak scenario developments for the next step. *Plasma Phys. Control. Fusion* **49**, B629.

JOFFRIN, E., CHALLIS, C.D., CONWAY, G.D., GARBET, X., GUDE, A., GÜNTER, S., HAWKES, N.C., HENDER, T.C., HOWELL, D.F. & HUYSMANS, G.T.A. 2003 Internal transport barrier triggering by rational magnetic flux surfaces in tokamaks. *Nucl. Fusion* **43**, 1167.

KERNER, W. & TASSO, H. 1982 Tearing mode stability for arbitrary current distribution. *Plasma Phys.* **24**, 97.

KWON, J.-M., HORTON, W., ZHU, P., MORRISON, P.J., PARK, H.-B. & CHOI, D.I. 2000 Global drift wave map test particle simulations. *Phys. Plasmas* **7**, 1169.

LICHTENBERG, A.J. & LIEBERMAN, M.A. 1997 *Regular and Chaotic Motion*, 2nd edn. Springer.

MACKAY, R.S., MEISS, J.D. & PERCIVAL, I.C. 1984 Transport in Hamiltonian systems. *Physica* D **13**, 55.

MARCUS, F.A., CALDAS, I.L., GUIMARÃES FILHO, Z.O., MORRISON, P.J., HORTON, W., KUZNETSOV, Y.K. & NASCIMENTO, I.C. 2008 Reduction of chaotic particle transport driven by drift waves in sheared flows. *Phys. Plasmas* **15**, 112304.

MARCUS, F.A., ROBERTO, M., CALDAS, I.L., ROSALEM, K.C. & ELSKENS, Y. 2019 Influence of the radial electric field on the shearless transport barriers in tokamaks. *Phys. Plasmas* **26**, 022302.

MAZZUCATO, E., BATHA, S.H., BEER, M., BELL, M., BELL, R.E., BUDNY, R.V., BUSH, C., HAHM, T.S., HAMMETT, G.W. & LEVINTON, F.M. 1996 Turbulent fluctuations in TFTR configurations with reversed magnetic shear. *Phys. Rev. Lett.* **77**, 3145.

MORRISON, P.J. 2000 Magnetic field lines, Hamiltonian dynamics, and nontwist systems. *Phys. Plasmas* **7**, 2279.

NASCIMENTO, I.C., KUZNETSOV, Y.K., SEVERO, J.H.F., FONSECA, A.M.M., ELFIMOV, A., BELLINTANI, V., MACHIDA, M., HELLER, M.V.A.P., GALVÃO, R.M.O. & SANADA, E.K. 2005 Plasma confinement using biased electrode in the TCABR tokamak. *Nucl. Fusion* **45**, 796.

OSORIO, L., ROBERTO, M., CALDAS, I.L., VIANA, R.L. & ELSKENS, Y. 2021 Onset of internal transport barriers in tokamaks. *Phys. Plasmas* **28**, 082305.

ROSALEM, K.C., ROBERTO, M. & CALDAS, I.L. 2014 Influence of the electric and magnetic shears on tokamak transport. *Nucl. Fusion* **54**, 064001.

ROSALEM, K.C., ROBERTO, M. & CALDAS, I.L. 2016 Drift-wave transport in the velocity shear layer. *Phys. Plasmas* **23**, 072504.

SIPS, A.C.C., *et al.* 2005 Advanced scenarios for ITER operation. *Plasma Phys. Control. Fusion* **47**, A19.

SZEZECH, J.D., CALDAS, I.L., LOPES, S.R., MORRISON, P.J. & VIANA, R.L. 2012 Effective transport barriers in nontwist systems. *Phys. Rev.* E **86**, 036206.

SZEZECH JR, J.D., CALDAS, I.L., LOPES, S.R., VIANA, R.L. & MORRISON, P.J. 2009 Transport properties in nontwist area-preserving maps. *Chaos* **19**, 043108.

TOUFEN, D.L., GUIMARÃES FILHO, Z.O., CALDAS, I.L., MARCUS, F.A. & GENTLE, K.W. 2012 Turbulence driven particle transport in Texas Helimak. *Phys. Plasmas* **19**, 012307.

VIEZZER, E., PÜTTERICH, T., CONWAY, G.D., DUX, R., HAPPEL, T., FUCHS, J.C., McDERMOTT, R.M., RYTER, F., SIEGLIN, B. & SUTTROP, W. 2013 High-accuracy characterization of the edge radial electric field at ASDEX Upgrade. *Nucl. Fusion* **53**, 053005.

WAGNER, F., BECKER, G., BEHRINGER, K., CAMPBELL, D., EBERHAGEN, A., ENGELHARDT, W., FUSSMANN, G., GEHRE, O., GERNHARDT, J. & GIERKE, G.V. 1982 Regime of improved confinement and high beta in neutral-beam-heated divertor discharges of the ASDEX tokamak. *Phys. Rev. Lett.* **49**, 1408.

WHITE, R.B. 2012 Modification of particle distributions by MHD instabilities I. *Commun Nonlinear Sci. Numer. Simul.* **17**, 2200.

WHITE, R.B. & CHANCE, M.S. 1984 Hamiltonian guiding center drift orbit calculation for plasmas of arbitrary cross section. *Phys. Fluids* **27**, 2455.

WOLF, R.C. 2002 Internal transport barriers in tokamak plasmas. *Plasma Phys. Control. Fusion* **45**, R1.

WURM, A., APTE, A., FUCHSS, K. & MORRISON, P.J. 2005 Meanders and reconnection–collision sequences in the standard nontwist map. *Chaos* **15**, 023108.

WURM, A. & MARTINI, K.M. 2013 Breakup of inverse golden mean shearless tori in the two-frequency standard nontwist map. *Phys. Lett.* A **377**, 622.

YUSHMANOV, P.N., TAKIZUKA, T., RIEDEL, K.S., KARDAUN, O.J.W.F., CORDEY, J.G., KAYE, S.M. & POST, D.E. 1990 Scalings for tokamak energy confinement. *Nucl. Fusion* **30**, 1999.

ZIMBARDO, G., POMMOIS, P. & VELTRI, P. 2000 The Kubo number as a parameter governing the level of chaos in magnetic turbulence. *Physica* A **280**, 99.